Reconstruction of the Fine-resolution Apparent Temperature (Humidex) With the Addition of Aerodynamic Parameters

Xilin Wu[1,2], Yong Ge[1,2,3*], Daoyi Gong[4] and Qingsheng Liu[1]

[1]State Key Laboratory of Resources and Environmental Information Systems, Institute of Geographic Sciences & Natural Resources Research, Chinese Academy of Sciences, Beijing 100101, China.

[2]University of Chinese Academy of Sciences, Beijing 100049, China. 3 Emergency Department of Peking University International Hospital, Beijing, China.

[3]Jiangsu Center for Collaborative Innovation in Geographical Information Resource Development and Application, Nanjing, 210023, China.

[4]Academy of Disaster Risk Science, Faculty of Geographical Science, Beijing Normal University, Beijing 100875, China

Corresponding author: Yong Ge (gey@lreis.ac.cn)

† 1 State Key Laboratory of Resources and Environmental Information Systems, Institute of Geographic Sciences & Natural Resources Research, Chinese Academy of Sciences, Beijing 100101, China

Key Points: HRMNSD; fine spatiotemporal resolution; aerodynamic parameters; mechanism fusion downscaling model

Abstract

The "felt temperature" is the preferred measure of hotness or coldness expressed to depict human sensory. However, to date, our perception of its spatial pattern with fine spatiotemporal data remains incomplete. Here, we demonstrated an empirical statistical approach incorporating atmospheric dynamics theory with aerodynamic parameters capable of developing hourly datasets at a high spatial resolution (0.01 x 0.01). This fusion mechanism model, named the Humidex Reconstruction Model based on Numerical Simulation Data (HRMNSD), employed reanalysis data and satellite data for both near surface temperature(Tair) and the dew point temperature(Tdew) to combine their respective advantages in the correct representation of a turbulent exchange between the surface and the atmosphere. We showed the good performance of this model in each season using the Yangtze River Delta, China as an example. The RMSEs of the Humidex were 2.47°C (in winter), 2.49°C (in spring), 2.80°C (in summer) and 2.56°C (in autumn), respectively.

1. Introduction

History shows that heat can be a ruthless killer. In 2021 alone, the death toll from the record-breaking heatwave that struck the United States and Canada rose to nearly 200 (Team, 2021). Over 166,000 people died from extreme temperatures from 1998 to 2017 (WHO, 2020).P prior literature (Founda and Santamouris, 2017) reveals the interactions and synergies between urban heat islands and heat waves and finding their positive feedback, which will increase the risk

of an urban population's exposure to heat. By 2020, 56.2% of the world's population was urban, and that proportion is projected to increase with rising incomes and shifts away from employment in agriculture (Ritchie and Roser, 2018). From a physiological perspective, extreme temperatures can acutely impact human health for short periods of time (WHO, 2018), often resulting in cascading respiratory and cardiovascular diseases and excess mortality. For example, heat exhaustion, the result of the body's overheating, is usually caused by exposure to high temperatures (particularly when combined with high humidity or strenuous physical activity) within several hours. It can lead to a life-threatening condition without prompt treatment. We currently lack a comprehensive, fine spatiotemporal resolution understanding of urban heat exposure (Shi et al.,2018; Tuholske et al.,2021). This shortcoming limits our ability to improve the urban living environment or to guide the development of functional early risk warning systems to accommodate heat exposure.

Temperature is a cornerstone of heat exposure recognition. Environmental health research usually decribes the thermal responses of humans as a wide range of metrics combined with such weather factors (Osczevski, 1995; Keimig and Bradley, 2002; Wilson, 1967; Rothfusz and Headquarters, 1990; Anderson et al., 2013; Ravagnolo et al., 2000; Budd, 2008; Zhang et al., 2016; Sirangelo et al., 2020; Błażejczyk et al., 2013), including the Wind Chill Index (WCI), Heat Index (HI), Wet Bulb Globe Temperature (WBGT), Humidex index, Universal Thermal Climate Index (UTCI), etc. The concept of "felt temperature" historically emerged to demonstrate that cold is felt more bitterly with a strong wind (Ecoten, 2020). Except for wind, the relative humidity of the air (Wan et al., 2009) and the mean radiant temperature (Kántor and Unger, 2011) are the key basic parameters determining human comfort. Among these indices, the Humidex (Wikipedia, 2015), which is widely used, is a relatively simple thermal comfort index combined with air temperature and humidity. In contrast with other models needing mean radiant temperature, it has much to recommend it, since its results can be directly comparable to the air temperature in degrees Celsius and are suitable for many branches of atmospheric science (Rozbicka and Rozbicki, 2020b; Pan et al., 2019; Oleson et al., 2015). Moreover, the Humidex is easier to understand and calculate, rendering it commonly used in the investigation of heat stress (Rainham and Smoyer-Tomic, 2003; Zamanian et al., 2017; Al-Bouwarthan et al., 2019; Smoyer-Tomic and Rainham, 2001).

In Humidex mapping, spatial interpolation, atmospheric simulation and statistical regression are three common strands of research. As the simplest method, spatial interpolation based on the first law of geography can generate air temperature (Stahl et al., 2006; DeGaetano and Belcher, 2007;Wang et al., 2017; Xu et al., 2018) and humidity (Geleyn et al., 1988; .Berndt andHaberlandt, 2018) maps with high spatial-temporal resolution, usually varying from several meters to kilometers on a spatial basis and an hour to a year on a temporal. However, it is affected by the distribution of points to be interpolated, resulting in considerable uncertainties and errors. An atmospheric simulation constructs mathematical models around primitive dynamic equations that control atmospheric

motion (Mistry and Malcolm, 2019). They can predict real-time processes on a multi-scale, including global flows (Gates, 1976), large-scale atmospheric circulation(Sandu et al., 2019), microscale weather forecasts (Wiersema, 2020), and sub-microscale turbulent flow over buildings (Auvinen et al., 2020; Tong et al., 2005). However, sub-micorscale is far from a satisfactory level in high-resolution mapping due to its complex parameter requirements, expansive time, and heavy operating load. Remote sensing data have excellent performance in providing spatially continuous, high-resolution geographic information. However, the land surface temperature (LST) retrieved from the thermal infrared data provided by satellite measurements cannot be used as an alternative to "felt temperature". These two interactive weather parameters differ, especially LST and air temperature, which are essential in Humidex calculation. Linear and nonlinear (Şahin, 2012; Shen et al., 2020; Li and Zha, 2018; Chen et al., 2015; Hjort et al., 2011) regression models were then built to estimate weather factors, such as air temperature and humidity, with observation sites and multiple environmental variables from satellites to reconstruct the "felt temperature" with its index function, as many researchers have done(Ho et al., 2016). For example, Hung et al. (2016) employed an empirical approach to map the apparent temperature (Humidex) by relying on meteorological observations and satellite layers combined in a random forest regression model. However, the satellite data present significant limitations for the estimations due to their inevitable cloud contamination and poor scanning frequency, making real-time monitoring unrealized.

Until now, the high-resolution mapping of the urban "felt temperature" (the Humidex was used in our study) has stayed in the observation-data-driven stage. There are two gaps in this observation-data-driven model in estimating meteorological parameters. First, it does not properly represent the turbulent exchange between the surface and atmosphere, especially over urban areas with their high-rise buildings and crisscrossing asphalt roads. Second, it has temporal resolution limitation, resulting in the weakness of capturing instantaneous heating that may cause injuries. To fill these gaps, we established an apparent temperature (Humidex) reconstruction model with fine spatial-temporal-resolution (hourly, 0.01 x 0.01), which is beyond the current level (daily, 1km x1km), combined the satellite data with fine-spatial resolution (0.01 x 0.01) with the ERA5 reanalysis data with fine-temporal resolution (hourly) and clear physical constraints,; and addedaerodynamic parameters (roughness length for natural surfaces and urban geometric characteristics for artificial surfaces). We named itthe Humidex Reconstruction Model based on Numerical Simulation Data (HRMNSD). Besides the Humidex, we presented a statistical downscaling model of the fusion mechanism for both near-surface temperature and dew point temperature that can offer basic data for many fields, such as climate change, agriculture, thermal health, etc.

2. Materials and Methodology

2.1 Data sources

All the data we used are publicly available. We supply their temporal and spatial resolutions here, tagged with their sources in Table S1. More details can be found in the descriptions given in the links.

2.2 Study area

The Yangtze Delta, one of China's three metropolitan regions, is a triangle-shaped metropolis centered on Shanghai. It is the most densely populated and concentrated industrial region and drives China's economic development, with the highest degree of regional integration and the most comprehensive transportation system. There may be more than 80 towns with various scales within 10,000 square kilometers. Although it accounts for only 2.2% of the total land area of China, the Yangtze Delta generated over 20% of China's GDP and was home to 16.7% of the national population at the end of 2020 (Dai et al., 2016). The Yangtze Delta is characterized by a marine monsoon subtropical climate, with hot and humid summers and cold and dry winters (Wikipedia, 2021). Extreme heat events occur frequently here due to the Western Pacific Subtropical High in the summer (Li et al., 2015). The rapid expansion of urbanization also creates a more intense heat wave for positive feedback (Wang et al., 2017).

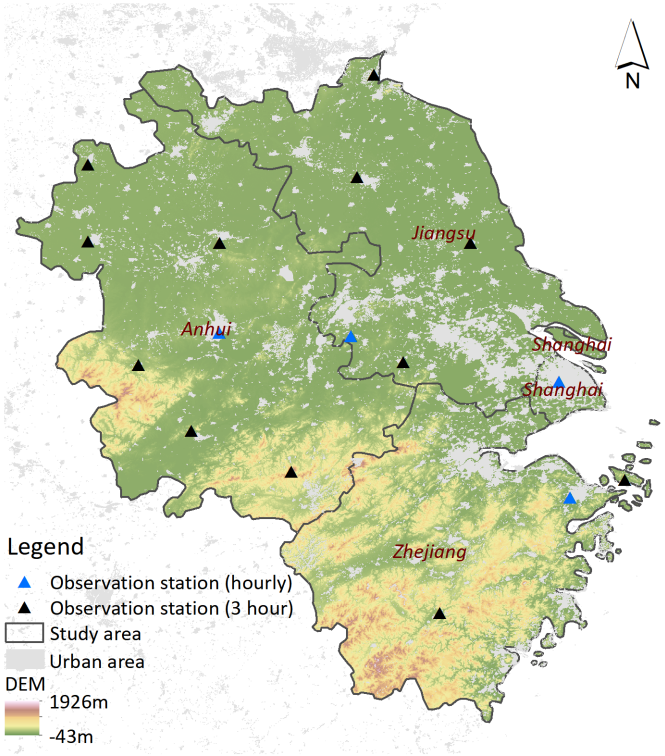

Figure 1. Overview of the Yangtze Delta and the distribution of meteorological stations according to NOAA. The blue triangles represent

the observation stations with hourly data, while the black triangles represent the observation stations that collect data every three hours.

2.3 Methodology

Combining satellite data and the theoreticaly framework of their physical processes (T*air* and T*dew*), we proposed various approaches for downscaling the reanalysis data, with the goal of reconstructing a high-accuracy, spatiotemporally continuous and fine-resolution (hourly, 0.01 x 0.01) apparent temperature (Humidex).

2.3.1 Data processing

We first eliminate the discontinuous satellite LST data (LST_{MODIS}) in time and space interfered with by cloud cover. A gap-filled method proposed by Shiff et al. (2021) was used to derive a spatiotemporally continuous LST (LST_c) dataset at a regional 1-km resolution of MODIS four times per day. The inconsistency in our study is the replacement of the numeric weather prediction model data (Climate Forecast System Version 2, CFSv2, for the original) with the ERA5 reanalysis hourly atmospheric variable (LST_{ERA5}).The core of this gap-filled model is derivingcloud-free seasonality (climatology) on a pixel-by-pixel basis using temporal Fourier analysis and filling the climatological gap with the anomaly data. Subsequently, we introduced a data fusion model (the enhanced spatial and temporal adaptive reflectance fusion model, ESTARFM; Zhu et al., 2010) to fuse satellite-based (LST_c, $TCWV_{MODIS}$) and ERA5-based (LST_{ERA5}, $TCWV_{ERA5}$) datasets, designed to generate LST and TCWV with fine resolution (hourly, 0.01 x 0.01). Here, the ERA5 product of 0.1 was simply resampled to 0.01 to run the ESTARFM. For the fused data,hourly continuous ERA5-based datasets providing information on time-series variations were used to reduce the systematic bias of the linear scaling model (Leander and Buishand, 2007) and the variance scaling model (Chen et al., 2011).

In the following pivotal step, two regression algorithms, named random forest (RF) and geographically weighted regression (GWR), were employed to downscale hourly ERA5-based T_{air} and T_{dew}.

For T_{air}, we split the data into two parts: the artificial surface and the natural surface. Two sets of covariates were used for urban (we called them the *artificial surface mechanism constrained downscaling indexes*, ASMCDI) and non-urbanized areas (*natural surface mechanism constrained downscaling indexes*, NSMCDI) respectively. For the natural surface, we finalized the covariates, including the leaf area index(LAI), the digital elevation model (DEM), and the roughness length for momentum (Z_{om}) and heat(Z_{oh}) via a procedure based on the Monin−Obukhov similarity theory, which represents the vertical exchange of heat, momentum, and moisture in the surface layer (Li et al., 2012). For artificial surfaces, three urban canopy geometry parameters under the framework of the urban canopy model (UCM; Cao and Lin, 2014) were used to replace the roughness length to characterize the impact of urban morphology on turbulent surface exchanges. The three geometry parameters are the plan area index ( ),

the canyon (floor and wall) frontal area index ($_c$), and the roof frontal area index ($_r$), which are necessary for the calculation of urban z_o parameterization schemes. Thus, we write the near-surface air temperature statistical downscaling models for a natural surface and an artificial surface as a nonlinear function, Eqs.(1) –(2), respectively:

$$T_{\text{air}} \propto F\left(T_{\text{surf}},\ DEM,\ LAI,\ z_o,\ e\right) \tag{1}$$

$$T_{\text{air}} \propto F\left(T_{\text{surf}},\ DEM,\ LAI,\ \eta\ , \lambda c,\ \lambda r\ ,\ e\right) \tag{2}$$

Where e is the residual caused by humidity and momentum fluctuations which is hard to quantify. The gravitational acceleration (g) decreases with altitude (DEM); z_o, including z_{om} and z_{oh}, is the surface roughness length used to measure the capacity of surface elements in absorbing momentum and heat. T_{surf} is the land surface temperature (we used the fusion LST_c here). The leaf area index (LAI) represents the size of the plant canopy. More details can be found in our supplemental information (SI). The RF algorithm was chosen here for two main reasons. One is its insensitivity to outlier disturbances (Robnik-Šikonja, 2004). The other is its advantage in handling complex nonlinear relationships (Auret and Aldrich, 2012).

For T_{dew}, the logarithmic correlation between the surface dew point temperature and the total amount of water vapor in the vertical air column was first proposed by Reitan (1963). Many studies have examined this relationship across geographic areas and confirmed that the correlation coefficient varies with season, latitude, and longitude (Smith, 1966; John, 1974; Viswanadham, 1981). Thus, the GWR model was applied to interpret this geographic dependence for the ERA5-based T*dew* scale conversion. The regression model here was written as Eq. (3):

$$T_{\text{dew}} = \ \beta_{1(xi,yi)} + \beta_{2(xi,yi)} \ln\left(\text{TCWV}\right)\ + \varepsilon_i \tag{3}$$

Where x_i,y_i is the parameter estimated at each location with the coordinates (x_i, y_i) and i is the residual of the ith location.We chose the adaptive kernel with the AICc estimated bandwidth in the process of model estimation. Notably, we assumed a scale-invariant relationship among variables on all the resolutions we used (0.1 and 0.01). We chose four days, including January 15, 2020 (winter), April 15, 2020 (spring), July 15, 2020 (summer) and October 15, 2020 (autumn), to test the seasonal performance of this method.

In the end, we reconstructed a fine-resolution apparent temperature using the Humidex formula and verified the accuracy of our results using hourly observation data. The validation results were the daily averages of each metric (correlation coefficient, r^2; mean absolute error, MAE; root mean square error,

RMSE; and Nash−Sutcliffe efficiency index, NSE) validated at all stations. Furthermore, we compared our accuracy with reanalysis-based data to obtain the downscaled model error, dropping out of the fixed error caused by the numeric simulation. All the formulas used in our model can be found in Supplmentary information.

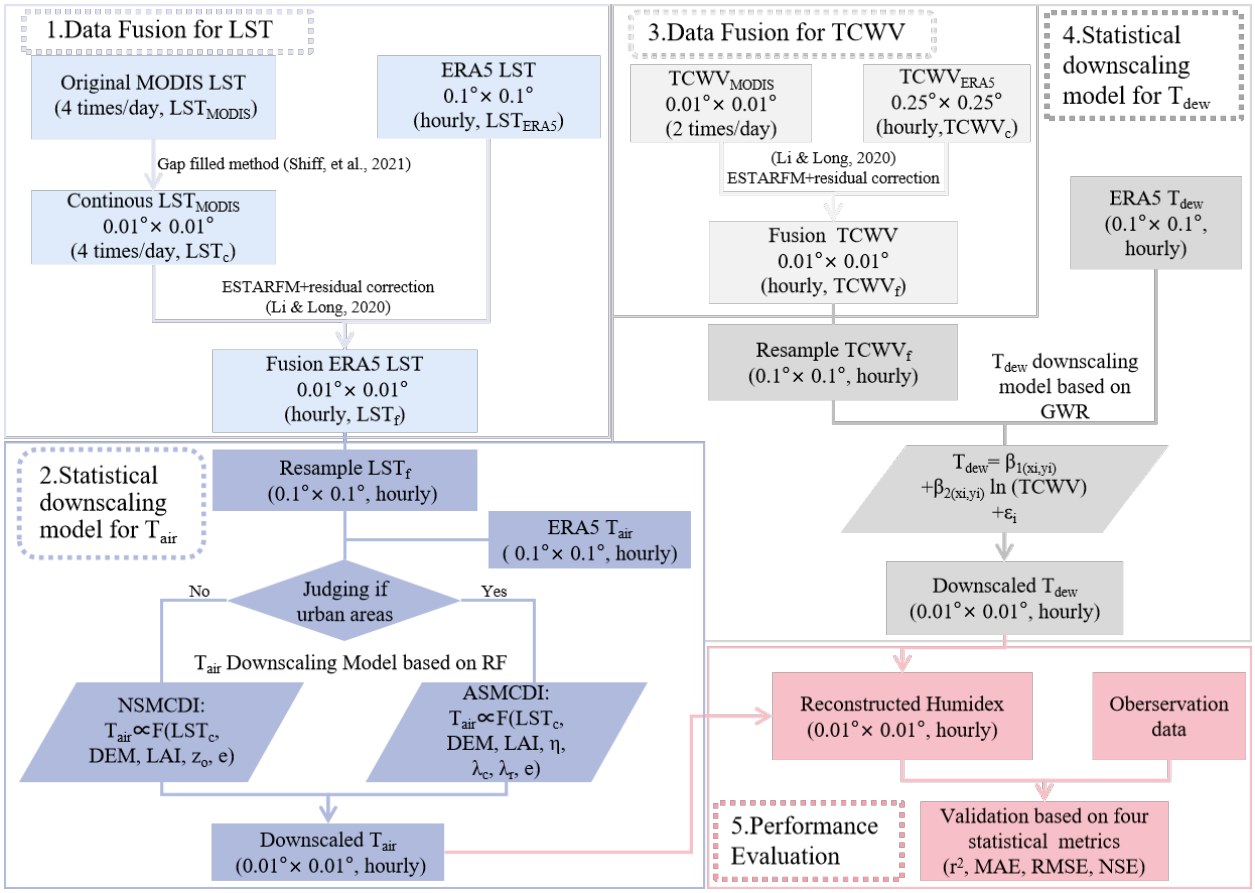

Figure 2. Flowchart of the Humidex reconstruction.

3. Results and Discussion

3.1 Accumulated errors of T_{air} and T_{dew} on the Humidex calculation

Table 1 summarizes the performances of downscaling models for both T_{air} and T_{dew} in all seasons based on the correlation coefficient (r^2), mean absolute error (MAE), root mean square error (RMSE) and Nash-Sutcliffe efficiency index (NSE). Basically, these seasonal downscaling T_{air} were good quality, with the MAE ranging from 1.6℃ to 1.9℃ and the RMSE which were generally lower than 2.5℃. The performance of T_{dew} can be divided into three grades: The T_{dew} downscaling model in winter achieved the best grade for its highest value

of r^2 (= 0.95) and its lowest value of RMSE(= 1.42℃); the model in spring and summer achieved the second grade for its relatively ideal correlation coefficient (> 0.6). Sometimes (for spring), there was a significantly lower RMSE(= 2.73℃) compared with the other three seasons. In autumn, the model made up the lowest grade for its poor value of r^2 To find the sources of errors, we listed the accuracy performance of the ERA5-based data and found their evident similarity to our downscaling results. This demonstrates our guaranteed data accuracy in data conversion from a coarse resolution (0.1 x0.1) to fine resolution (0.01 x 0.01).

To further understand the effect of cumulative transfer errors from the downscaled T_{air} and T_{dew} on the Humidex calculation, we drew a violin plot that visualized the distribution of both observed and predicted numeric data. Figure B1 illustrates such a phenomenon: If the distribution of predicted data was like the observed one, the Humidex also showed the same characteristic, regardless of the poor quality of T_{dew};. Under the opposite conditions, there were slightly different patterns in their distributions. This means that the accuracy of the predicted T_{dew} did not have a significant effect on the final calculation of the Humidex. Table 2 verifies this phenomenon with a similar MAE and RMSE for each season.

Table 1. Validation accuracy for downscaling T_{air}, downscaling T_{dew}, a reconstructed Humidex, ERA5-based T_{air} and ERA5-based T_{dew} in each season. Accuracy is given by MAE, RMSE, r^2, and NSE.

Date	01.15	04.15	07.15	10.15	Date	01.15	04.15	07.15	10.15
MAE					r^2				
T_{air}	1.87	1.68	1.82	1.62	T_{air}	0.81	0.93	0.81	0.81
T_{dew}	1.08	1.97	1.12	1.25	T_{dew}	0.95	0.82	0.88	0.59
Humidex	1.93	1.59	2.11	1.91	Humidex	0.83	0.90	0.74	0.66
ERA5-based T_{air}	1.07	1.90	1.10	1.18	ERA5-based T_{air}	0.93	0.92	0.88	0.86
ERA5-based T_{dew}	1.01	1.92	1.07	1.17	ERA5-based T_{dew}	0.95	0.85	0.85	0.63
Date	01.15	04.15	07.15	10.15	Date	01.15	04.15	07.15	10.15
RMSE					NSE				
T_{air}	2.42	2.32	2.46	2.16	T_{air}	0.53	0.79	0.22	0.47
T_{dew}	1.42	2.73	1.56	1.66	T_{dew}	0.84	0.31	0.27	-0.19
Humidex	2.47	2.49	2.80	2.56	Humidex	0.68	0.80	0.47	0.39
ERA5-based T_{air}	1.33	2.62	1.58	1.75	ERA5-based T_{air}	0.86	0.73	0.68	0.65
ERA5-based T_{dew}	1.34	2.58	1.43	1.52	ERA5-based T_{dew}	0.86	0.38	0.39	-0.01

3.2 Spatial pattern comparison of T_{air} and Humidex

Based on the HRMNSD scheme described in the methodology section, the final products of Humidex were made for the four experimental dates once hourly. In Figure 3, we aggregated the daily mean Humidex and T_{air}, and given an overview box plot on each single day to illustrate their hourly spatial variations

based on the basic five-number summary (minimum, first quartile, median, third quartile, maximum) on each single day. The hourly data are shown in SI (Fig. B2-B13).

Through this figure, we can easily find the similarities and variations of the spatial pattern between the Humidex and T_{air}: In winter (January 15), the Humidex was generally lower than the air temperature, with a 2.3℃ difference in the daily mean temperature. In spring (April 15), there were striking resemblances between the felt temperature (Humidex) and the actual temperature (T_{air}, with differences in the daily mean value within 1℃). Spatially, the North was where the warmth was the most pronounced. In summer (July 15), the daily mean value was 33.3°C(minimum: 27.0°C, maximum: 43.6°C) of the Humidex and 24.4°C(minimum: 19.9°C, maximum: 30.5°C) of the air temperature, showing a huge gap ($>$ 10℃) all day long. In autumn (October 15), the fluctuations of "felt" and "actual" temperatures were mainly concentrated from morning to noon when the daily average varied within 5℃. For the whole area, the temperature (both humidex and T_{air}) was relatively higher in the South closer to the coastline except during spring. The Humidex showed a visible spatial pattern, roughly dividing the study area into two zones: a hot zone (in Zhejiang and Shanghai) and a relatively cool zone (in Jiangsu and Anhui).

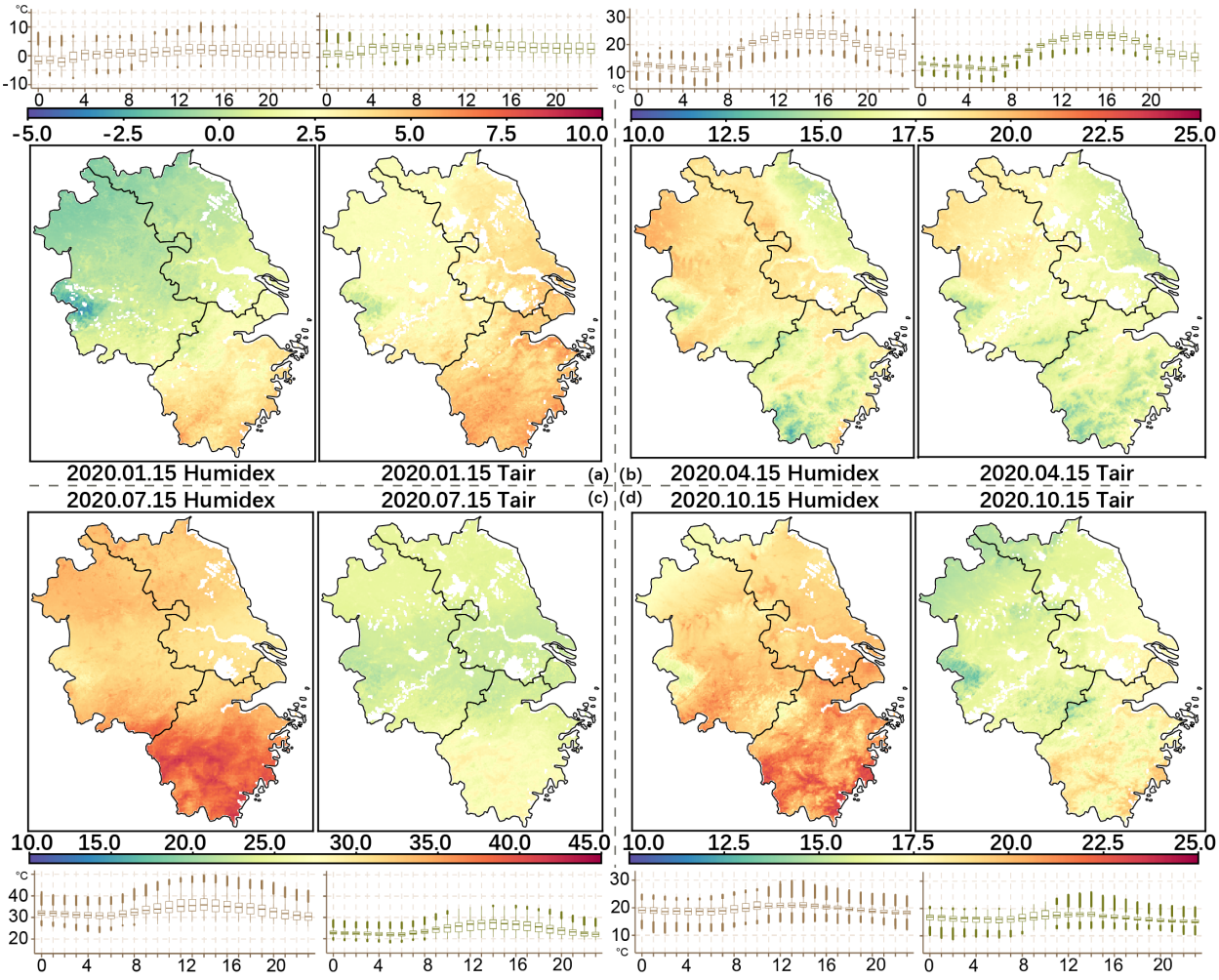

Figure 3. Spatial pattern of reconstructed Humidex and downscaled T_{air} on (a) January 15, 2020; (b) April 15, 2020; (c) July 15, 2020; and (d) October 15, 2020. Within each subfigure, the daily average Humidex product was put on the left with its hourly variation box plot at the top/bottom and the T_{air} product was put on the right with its hourly variation box plot at the top/bottom. The legend is shared within each subfigure.

3.3 Uncertainty and limitations

Generally, the accuracy of weather parameter estimation (such as air temperature, humidity, etc.) always decreases in parallel with finer temporal and spatial resolutions. Taking air temperature as an example, Zhu et al. (2013) reported an RMSE of 2.97℃ for the 1-km daily minimum air temperature estimation (7.45℃ for the daily maximum air temperature), whereas Serra et al. (2020)

provided the statistically derived 1-km air temperature at annual, seasonal, and monthly scales, whose RMSE varies from 1.5-2.0℃ (annual), from 1.3-2.0℃ (seasonal) and from 1.2-2.1℃ (monthly), respectively. In addition, Hooker et al. (2018) developed a dataset of monthly air temperatures at a spatial resolution of 0.05 (about 5-km) with the RMSE varying from 1.0 to 2.2℃. Compared with the product using the statistical model, simulation techniques generally produce the air temperature mapping with high temporal resolution and ideal accuracy (RMSE ranging from 0.5 to 3℃; Masunaga et al., 2018; He et al., 2020), but rarely in a micro scale (about 1 km or less) because of the high computational cost. The air temperature product presented in our study has an RMSE of less than 2.5℃ (ranging from 2.16 to 2.47℃), which is similar to (or even better than) the daily-resolution product. For the Humidex,mapping with fine spatial-temporal resolution is rare but more closely related to heat mortality. For example, Hung et al. (2016) presented a method to estimate the daily Humidex whose RMSE was equal to 2.04℃. The performance of our study (RMSE: 2.34-2.80℃) is broadly similar, but provides a finer temporal resolution (hourly). What needs to be emphasized is that there are some inevitable limitations and incomparability among these comparisons over their performance accuracy for the diversity of their data, model and study area. Broadly speaking, our method conferred a great improvement on the temporal resolution and filled the hourly data gap of air temperature, dew point temperature, and Humidex in a micro scale (kilometer- level) without cutting the high degree of accuracy of numeric simulation data.

Far more than the stability and accuracy performance, weather parameters predicted by numeric simulation have a clearer constraint condition on climate dynamical mechanisms (Kumar et al., 2021; Zhang et al., 2022), which is also proof of choosing the input parameters in our study. In previous studies, the LST (Zhang et al., 2016; Zhang et al., 2018; Colombi et al., 2007; Benali et al., 2012; Vancutsem et al., 2010; Weng, 2009; Sohrabinia et al., 2015; Mutiibwa et al., 2015; Cao et al., 2021; Zakšek and Schroedter-Homscheidt, 2009; Oyler et al., 2016), Normalized Difference Vegetation Index (NDVI; Nieto et al., 2011; Hassaballa and Matori, 2011), DEM (Huang et al., 2017), Distance to Coast (dos Santos, 2020; Good, 2015), Solar Zenith Angle (Cresswell et al., 1999; Jang et al., 2004), Julian day (Jang et al., 2004; Emamifar et al., 2013; Janatian et al., 2017), altitude (Janatian et al., 2017) and the like are the common auxiliary variables for T_{air} estimation using advanced statistical methods. Scholars use these parameters considering the environmental factors affecting the land atmosphere exchange and their performance reported in the literature instead of the general atmospheric circulation. We confirmed that the selection of the above variables is absolutely right, whereas it may increase the computational cost with the inexact boundary conditions. The parameters selected through the ECMWF land surface mechanism may present more proper constraints along with simplifying T_{air} estimation rather than significantly improving accuracy. In this study, we established a statistically downscaled model based on the reanalysis data without correcting its systematic error in the pre-process. This

may highlight the inconsistency of the punctual measurements observed by the weather station. The main question is: A pixel with coarse resolution (0.1 x 0.1) is quite heterogeneous; it describes a more complex surface around the finite environment measured by the ground station. This means thatpunctual measurements may not be representative of the corresponding reanalysis pixels. In other words, the systematic error of the reanalysis data will transfer along with the downscaling, weakening our model.

Another weakness of the HRMNSD is its instability in complex mountainous terrain or snow and ice cover. Of course, turbulence is generally a characteristic of the interaction between atmospheric flow and the surface (friction and exchange of thermal, or radiative, energy; Sun et al., 2015; Wyngaard, 1992). When turbulence circulates among complex mountains, the varied of terrain makes the stratified atmosphere unstable, which further enhances or reduces heat or energy transport (North, 1975). Even in large-scale numeric models, the parameterization of topography-specific regional effects is still missing (Lehner and Rotach, 2018). An example of poor model performance in mountainous terrain is atmospheric stability, particularly during cold-air pool episodes, often leading to an underestimation of inversion strength and an overestimation of near-surface temperatures (Lehner and Rotach, 2018). Moreover, the exchange between land surface and atmosphere is also influenced by snow albedo feedback processes (Letcher and Minder, 2015; Bishop et al., 2011). Therefore, the weather parameter downscaling of complex mountainous terrain or of snow and ice coverage is more challenging than the current model. Fortunately, extreme heat events generally do not originate in these areas. This makes our model sufficiently applicable for assessing the heat exposure of inhabitants.

5. Conclusion

Our study provided a feasible scheme for reconstructing a Humidex map with fine spatial-temporal resolution (hourly, 0.01 x0.01) by combining the individual advantages of numeric simulation and remote sensing. The accuracy of our model is ideal with the population RMSE ranging from 2.47-2.80℃, MAE ranging from 1.59-2.11℃, r^2 ranging from 0.66-0.92 and NSE ranging from 0.39-0.80 for the four seasons. Furthermore, we found a diverse spatial pattern between the near surface temperature and the Humidex (in seasons such as winter and summer), which revealed that water vapor is a strong weather component in the temperature "felt" by the human body to be reckoned with. In the future, we may reproduce our work in more complex scenarios, such as ice coverage and rugged terrain. We can map the global dataset with an improved realistic surface roughness length. Where technically feasible, we can even simulate the intensity and direction of wind fields and the duration of sunlight to optimize the mapping of "felt temperature". More comprehensive datasets could also be made to cater to more studies based on "felt temperature" metrics for various exposures of all kinds of biological groups (e.g. humans, plants, and animals).

Acknowledgments

The authors thank the GEE code development team Shiff, S., Helman, D., and Lensky, I. M for their assistance in providing the calculation code of global continuous LST. All the ERA5-Land data used in our work generated using *Copernicus Climate Change Service Information* [2020]

This research work was jointly financially supported by the Strategic Priority Research Program of Chinese Academy of Sciences, Grant No. XDA 20030302, and the National Natural Science Foundation for Distinguished Young Scholars of China (No. 41725006). The authors would like to thank the editor and anonymous reviewers for their comments and suggestions that have helped us improve the final manuscript.

Open Research

Data Availability Statement

All the data included in this work are publical availiable and free. Land surface temperature data, land cover data, total column water vapor data, leaf area index data were available from the Level-1 and Atmosphere Archive & Distribution System (LAADS) Distributed Active Archive Center (DAAC) through https://ladsweb.modaps.eosdis.nasa.gov/. ERA5-skin temperarture data, near surface temperature data, total column water vapor data and dew point temperature data were available from Copernicus Climate Change Service (C3S) Climate Data Store (CDS) at https://cds.climate.copernicus.eu/cdsapp#!/home. Observation data used to validation was downloaded from the National Centers for Environmental Infromation, available at https://www.ncei.noaa.gov/maps /hourly/. 30-meter digital elevation data from the Shuttle Radar Topography Mission was available at https://dwtkns.com/srtm30m/. 30-meter ALOS global digital surface model data was supported by ALOS Science Project, Earth Observation Research Center (EORC), Japan Aerospace Exploration Agency (JAXA), available at https://www.eorc.jaxa.jp/ALOS/en/aw3d30/terms.htm.

References

Al-Bouwarthan, M., Quinn, M. M., Kriebel, D., & Wegman, D. H. (2019). Assessment of heat stress exposure among construction workers in the hot desert climate of Saudi Arabia. *Annals of work exposures and health, 63(5)*, 505-520. doi: 10.1093/annweh/wxz033.

Auret, L., & Aldrich, C. (2012). Interpretation of nonlinear relationships between process variables by use of random forests. *Minerals Engineering, 35*, 27-42. doi: 10.1016/j.mineng.2012.05.008.

Auvinen, M., Boi, S., Hellsten, A., Tanhuanpää, T., & Järvi, L. (2020). Study of realistic urban boundary layer turbulence with high-resolution large-eddy simulation. *Atmosphere, 11(2)*, 201.doi: 10.3390/atmos11020201.

Tong, H., Walton, A., Sang, J., & Chan, J. C. (2005). Numerical simulation of the urban boundary layer over the complex terrain of Hong Kong. *Atmospheric environment, 39(19)*, 3549-3563.doi: 10.1016/j.atmosenv.2005.02.045.

Benali, A., Carvalho, A. C., Nunes, J. P., Carvalhais, N., & Santos, A. (2012). Estimating air surface temperature in Portugal using MODIS LST data. *Remote Sensing of Environment, 124*, 108-121.doi: 10.1016/j.rse.2012.04.024.

Bishop, M. P., Björnsson, H., Haeberli, W., Oerlemans, J., Shroder, J. F., & Tranter, M. (2012). Encyclopedia of snow, ice and glaciers.*Reference Reviews, 26(2)*, 40-41. doi: 10.1108/09504121211205241.

Rozbicka, K., & Rozbicki, T. (2020b). Long-term variability of bioclimatic conditions and tourism potential for Warsaw agglomeration (Poland). *International Journal of Biometeorology, 65(9)*, 1485–1495. doi: 10.1007/s00484-020-01957-2.

Pan, R., Gao, J., Wang, X., Bai, L., Wei, Q., Yi, W., ... & Su, H. (2019). Impacts of exposure to humidex on the risk of childhood asthma hospitalizations in Hefei, China: Effect modification by gender and age. *Science of the Total Environment, 691*, 296-305. doi: 10.1016/j.scitotenv.2019.07.026.

Oleson, K. W., Monaghan, A., Wilhelmi, O., Barlage, M., Brunsell, N., Feddema, J., ... & Steinhoff, D. F. (2015). Interactions between urbanization, heat stress, and climate change. *Climatic Change, 129(3)*, 525-541. doi: 10.1007/s10584-013-0936-8.

Budd, G. M. (2008). Wet-bulb globe temperature (WBGT)—its history and its limitations. *Journal of Science and Medicine in Sport, 11(1)*, 20-32. doi: 10.1016/j.jsams.2007.07.003.

Zhang, W., Du, Z., Zhang, D., Yu, S., Huang, Y., & Hao, Y. (2016). Assessing the impact of humidex on HFMD in Guangdong Province and its variability across social-economic status and age groups. *Scientific reports, 6(1)*, 1-8. doi: 10.1038/srep18965

Sirangelo, B., Caloiero, T., Coscarelli, R., Ferrari, E., & Fusto, F. (2020). Combining stochastic models of air temperature and vapour pressure for the analysis of the bioclimatic comfort through the Humidex. *Scientific Reports, 10(1)*, 1-16. doi: 10.1038/s41598-020-68297-4

Błażejczyk, K., Jendritzky, G., Bröde, P., Fiala, D., Havenith, G., Epstein, Y., ... & Kampmann, B. (2013). An introduction to the universal thermal climate index (UTCI). *Geographia Polonica, 86(1)*, 5-10. doi: 10.7163/gpol.2013.1.

Cao, J., Zhou, W., Zheng, Z., Ren, T., & Wang, W. (2021). Within-city spatial and temporal heterogeneity of air temperature and its relationship with land surface temperature. *Landscape and Urban Planning, 206*, 103979. doi: 10.1016/j.landurbplan.2020.103979.

Cresswell, M. P., Morse, A. P., Thomson, M. C., & Connor, S. J. (1999). Estimating surface air temperatures, from Meteosat land surface temperatures, using an empirical solar zenith angle model. *International Journal of Remote Sensing, 20(6)*, 1125-1132. doi: 10.1080/014311699212885.

Dai, L., Derudder, B., Liu, X., Ye, L., & Duan, X. (2016). Simulating infrastructure networks in the Yangtze River Delta (China) using generative urban network models. Belgeo. *Revue belge de géographie, (2)*. doi: 10.4000/belgeo.17087.

dos Santos, R. S. (2020). Estimating spatio-temporal air temperature in London (UK) using machine learning and earth observation satellite data. *International Journal of Applied Earth Observation and Geoinformation, 88*, 102066. doi: 10.1016/j.jag.2020.102066

ECMWF, S. P. (2014). In IFS documentation CY40R1 Part IV: Physical Processes. *ECMWF: Reading, UK,* 111-113. doi: 10.21957/8o7vwlbdr

Ecoten. (2020). Extreme Heat: understand the metrics behind "felt temperature" – Urban Comfort. doi: https://urban-comfort.eu/extreme-heat-understand-the-metrics-behind-felt-temperature/.

Founda, D., & Santamouris, M. (2017). Synergies between Urban Heat Island and Heat Waves in Athens (Greece), during an extremely hot summer (2012). *Scientific reports, 7(1)*, 1-11. doi: https://doi.org/10.1038/s41598-017-11407-6.

Gates, W. L. (1976). The numerical simulation of ice-age climate with a global general circulation model. *Journal of Atmospheric Sciences, 33(10)*, 1844-1873. doi: 10.1016/0146-6291(77)90282-x..

Geleyn, J. F. (1988). Interpolation of wind, temperature and humidity values from model levels to the height of measurement. *Tellus A, 40(4)*, 347-351. doi: 10.1111/j.1600-0870.1988.tb00352.x.

Berndt, C., & Haberlandt, U. (2018). Spatial interpolation of climate variables in Northern Germany—Influence of temporal resolution and network density. *Journal of Hydrology: Regional Studies, 15*, 184-202. doi: 10.1016/j.ejrh.2018.02.002.

Good, E. (2015). Daily minimum and maximum surface air temperatures from geostationary satellite data. *Journal of Geophysical Research: Atmospheres, 120(6)*, 2306-2324. doi: 10.1002/2014jd022438.

Ho, H. C., Knudby, A., Xu, Y., Hodul, M., & Aminipouri, M. (2016). A comparison of urban heat islands mapped using skin temperature, air temperature, and apparent temperature (Humidex), for the greater Vancouver area. *Science of the Total Environment, 544*, 929-938. doi: 10.1016/j.scitotenv.2015.12.021.

Hooker, J., Duveiller, G., & Cescatti, A. (2018). A global dataset of air temperature derived from satellite remote sensing and weather stations. *Scientific data, 5(1)*, 1-11. doi: 10.1038/sdata.2018.246.

Huang, F., Ma, W., Wang, B., Hu, Z., Ma, Y., Sun, G., ... & Lin, Y. (2017). Air temperature estimation with MODIS data over the Northern Tibetan Plateau. Advances in Atmospheric *Sciences, 34(5)*, 650-662. doi:10.1007/s00376-016-6152-5.

Jang, J. D., Viau, A. A., & Anctil, F. (2004). Neural network estimation of air temperatures from AVHRR data. *International Journal of Remote Sensing, 25(21)*, 4541-4554.doi: 10.1080/01431160310001657533.

Kántor, N., & Unger, J. (2011). The most problematic variable in the course of

human-biometeorological comfort assessment—the mean radiant temperature. *Central European Journal of Geosciences, 3(1)*, 90-100. doi: 10.2478/s13533-011-0010-x.

Kumar, S., Panda, B., & Raju, P. V. S. (2021). Numerical Simulation of Heavy Rainfall Using Weather Research and Forecast (WRF) System. In Proceedings of International Conference on Scientific and Natural Computing (pp. 127-136). *Springer, Singapore*. doi: 10.1007/978-981-16-1528-3_11.

Zhang, M., Zhou, C., Zhang, J., Zhang, X., & Tang, Z. (2022). Numerical Simulation and Analysis of Storm Surges Under Different Extreme Weather Event and Typhoon Experiments in the South Yellow Sea. *Journal of Ocean University of China, 21(1),* 1-14. doi:10.1007/s11802-022-4750-7.

Lehner, M., & Rotach, M. W. (2018). Current challenges in understanding and predicting transport and exchange in the atmosphere over mountainous terrain. *Atmosphere, 9(7)*, 276. doi: 10.3390/atmos9070276.

Letcher, T. W., & Minder, J. R. (2015). Characterization of the simulated regional snow albedo feedback using a regional climate model over complex terrain. *Journal of Climate, 28(19),* 7576-7595. doi:10.1175/jcli-d-15-0166.1.

Li, D., Bou-Zeid, E., & De Bruin, H. A. (2012). Monin–Obukhov similarity functions for the structure parameters of temperature and humidity. *Boundary-layer meteorology, 145(1)*, 45-67. doi: 10.1007/s10546-011-9660-y.

Cao, M., & Lin, Z. (2014). Impact of urban surface roughness length parameterization scheme on urban atmospheric environment simulation. *Journal of Applied Mathematics, 2014*. doi: 10.1155/2014/267683.

Li, J., Ding, T., Jia, X., & Zhao, X. (2015). Analysis on the extreme heat wave over China around Yangtze River region in the summer of 2013 and its main contributing factors. *Advances in Meteorology, 2015*. doi: 10.1155/2015/706713

Masunaga, R., Nakamura, H., Kamahori, H., Onogi, K., & Okajima, S. (2018). JRA-55CHS: An atmospheric reanalysis produced with high-resolution SST. *Sola, 14*, 6-13. doi: 10.2151/sola.2018-002.

He, J., Yang, K., Tang, W., Lu, H., Qin, J., Chen, Y., & Li, X. (2020). The first high-resolution meteorological forcing dataset for land process studies over China. *Scientific Data, 7(1)*, 1-11. doi: 10.1038/s41597-020-0369-y.

Maynard, K., & Royer, J. F. (2004). Sensitivity of a general circulation model to land surface parameters in African tropical deforestation experiments. *Climate Dynamics, 22(6)*, 555-572. doi: 10.1007/s00382-004-0398-9.

Mistry, M. N. (2020). A High Spatiotemporal Resolution Global Gridded Dataset of Historical Human Discomfort Indices. Atmosphere, 11(8), 835. doi:10.3390/atmos11080835.

Muñoz Sabater, J., (2021): ERA5-Land hourly data from 1950 to 1980. *Copernicus Climate Change Service (C3S) Climate Data Store (CDS)*.doi: 10.24381/cds.e2161bac

Janatian, N., Sadeghi, M., Sanaeinejad, S. H., Bakhshian, E., Farid, A., Hasheminia, S. M., & Ghazanfari, S. (2017). A statistical framework for estimating air temperature using MODIS land surface temperature data. *International Journal of Climatology, 37(3)*, 1181-1194. doi: 10.1002/joc.4766.

Mutiibwa, D., Strachan, S., & Albright, T. (2015). Land surface temperature and surface air temperature in complex terrain. *IEEE Journal of Selected Topics in Applied Earth Observations and Remote Sensing, 8(10)*, 4762-4774. doi : 10.1109/jstars.2015.2468594.

Nelli, N. R., Temimi, M., Fonseca, R. M., Weston, M. J., Thota, M. S., Valappil, V. K., ... & Al Naqbi, H. (2020). Impact of roughness length on WRF simulated land-atmosphere interactions over a hyper-arid region. *Earth and Space Science, 7(6),* e2020EA001165. doi: 10.1029/2020ea001165.

Nieto, H., Sandholt, I., Aguado, I., Chuvieco, E., & Stisen, S. (2011). Air temperature estimation with MSG-SEVIRI data: Calibration and validation of the TVX algorithm for the Iberian Peninsula. *Remote Sensing of Environment, 115(1)*, 107-116. doi: 10.1016/j.rse.2010.08.010.

Hassaballa, A. A., & Matori, A. B. (2011). The estimation of air temperature from NOAA/AVHRR images and the study of NDVI-Ts impact: Case study: The application of split-window algorithms over (Perak Tengah & Manjong) area, Malaysia. *In Proceeding of the 2011 IEEE international conference on space science and communication (IconSpace) (pp. 20-24)*. IEEE. doi: 10.1109/IConSpace.2011.6015844.

North, G. R. (1975). Analytical solution to a simple climate model with diffusive heat transport. *Journal of Atmospheric Sciences, 32(7)*, 1301-1307. doi: 10.1175/1520-0469(1975)032<1301:ASTASC>2.0.CO;2.

Osczevski, R. J. (1995). The Basis of windchill, *Arctic, 48*, 372-382. doi: 10.14430/arctic1262

Keimig, F.T. and Bradley, R. (2002). Recent changes in wind chill temperatures at high latitudes in North America, *Geophysical Research Letters, 29 (8)*. doi: 10.1029/2001gl013228.

Oyler, J. W., Dobrowski, S. Z., Holden, Z. A., & Running, S. W. (2016). Remotely sensed land skin temperature as a spatial predictor of air temperature across the conterminous United States. *Journal of Applied Meteorology and Climatology, 55(7)*, 1441-1457. doi: 10.1175/jamc-d-15-0276.1.

Rainham, D. G., & Smoyer-Tomic, K. E. (2003). The role of air pollution in the relationship between a heat stress index and human mortality in Toronto. *Environmental research, 93(1)*, 9-19. doi: 10.1016/s0013-9351(03)00060-4

Reitan, C. H. (1963). Surface dew point and water vapor aloft. *Journal of Applied Meteorology (1962-1982)*, 776-779. doi: 10.1175/1520-0450(1963)002<0776:sdpawv>2.0.co;2

Ritchie, H., & Roser, M. (2018). Urbanization. *Published online at OurWorldInData.org.* https://ourworldindata.org/urbanization.

Robnik-Šikonja, M. (2004). Improving random forests. *In European conference on machine learning (pp. 359-370).* Springer, Berlin, Heidelberg. doi:

Şahin, M. (2012). Modelling of air temperature using remote sensing and artificial neural network in Turkey. *Advances in space research, 50(7)*, 973-985. doi: 10.1016/j.asr.2012.06.021.

Shen, H., Jiang, Y., Li, T., Cheng, Q., Zeng, C., & Zhang, L. (2020). Deep learning-based air temperature mapping by fusing remote sensing, station, simulation and socioeconomic data. *Remote Sensing of Environment, 240*, 111692. doi: 10.1016/j.rse.2020.111692.

Li, L., & Zha, Y. (2018). Mapping relative humidity, average and extreme temperature in hot summer over China. *Science of the Total Environment, 615,* 875-881. doi 10.1016/j.scitotenv.2017.10.022

Chen, F., Liu, Y., Liu, Q., & Qin, F. (2015). A statistical method based on remote sensing for the estimation of air temperature in China. *International Journal of Climatology, 35(8)*, 2131-2143. doi: 10.1002/joc.4113

Hjort, J., Suomi, J., & Käyhkö, J. (2011). Spatial prediction of urban–rural temperatures using statistical methods. *Theoretical and applied climatology, 106(1)*, 139-152. doi :10.1007/s00704-011-0425-9.

Sandu, I., van Niekerk, A., Shepherd, T. G., Vosper, S. B., Zadra, A., Bacmeister, J., ... & Svensson, G. (2019). Impacts of orography on large-scale atmospheric circulation. *npj Climate and Atmospheric Science, 2(1)*, 1-8. doi: 10.1038/s41612-019-0065-9.

Serra, C., Lana, X., Martínez, M. D., Roca, J., Arellano, B., Biere, R., ... & Burgueno, A. (2020). Air temperature in Barcelona metropolitan region from MODIS satellite and GIS data. *Theoretical and Applied Climatology, 139(1-2)*, 473-492. doi:10.1007/s00704-019-02973-y.

Shi, Y., Katzschner, L., & Ng, E. (2018). Modelling the fine-scale spatiotemporal pattern of urban heat island effect using land use regression approach in a megacity. *Science of the Total Environment, 618*, 891-904. doi: 10.1016/j.scitotenv.2017.08.252.

Shiff, S., Helman, D., & Lensky, I. M. (2021). Worldwide continuous gap-filled MODIS land surface temperature dataset. *Scientific Data, 8(1)*, 1-10. doi: 10.1038/s41597-021-00861-7.

Smoyer-Tomic, K. E., & Rainham, D. G. (2001). Beating the heat: development and evaluation of a Canadian hot weather health-response plan. *Environmental health perspectives, 109(12)*, 1241-1248. doi: 10.1289/ehp.011091241.

Sohrabinia, M., Zawar-Reza, P., & Rack, W. (2015). Spatio-temporal analysis of the relationship between LST from MODIS and air temperature in New Zealand. *Theoretical and applied climatology, 119(3)*, 567-583. doi: 10.1007/s00704-014-1106-2.

Stahl, K., Moore, R. D., Floyer, J. A., Asplin, M. G., & McKendry, I. G. (2006). Comparison of approaches for spatial interpolation of daily air temperature in a large region with complex topography and highly variable station density. *Agricultural and forest meteorology, 139(3-4)*, 224-236. doi: 10.1016/j.agrformet.2006.07.004.

DeGaetano, A. T., & Belcher, B. N. (2007). Spatial interpolation of daily maximum and minimum air temperature based on meteorological model analyses and independent observations. *Journal of Applied Meteorology and Climatology, 46(11)*, 1981-1992. doi 10.1175/2007jamc1536.1.

Wang, M., He, G., Zhang, Z., Wang, G., Zhang, Z., Cao, X., ... & Liu, X. (2017). Comparison of spatial interpolation and regression analysis models for an estimation of monthly near surface air temperature in China. *Remote Sensing, 9(12)*, 1278. doi: 10.3390/rs9121278.

Xu, C., Wang, J., & Li, Q. (2018). A new method for temperature spatial interpolation based on sparse historical stations. *Journal of Climate, 31(5)*, 1757-1770. doi: 10.1175/jcli-d-17-0150.1.

Sun, J., Nappo, C. J., Mahrt, L., Belušić, D., Grisogono, B., Stauffer, D. R., ... & Neff, W. D. (2015). Review of wave-turbulence interactions in the stable atmospheric boundary layer. *Reviews of geophysics, 53(3)*, 956-993. doi: 10.1002/2015RG000487.

Team, W. W. (2021). US Pacific north-west heatwave killed almost 200 people. *WION*. doi: https://www.wionews.com/world/us-pacific-north-west-heatwave-killed-almost-200-people-396895.

Tuholske, C., Caylor, K., Funk, C., Verdin, A., Sweeney, S., Grace, K., ... & Evans, T. (2021). Global urban population exposure to extreme heat. *Proceedings of the National Academy of Sciences, 118(41)*. doi: 10.1073/pnas.2024792118.

Vancutsem, C., Ceccato, P., Dinku, T., & Connor, S. J. (2010). Evaluation of MODIS land surface temperature data to estimate air temperature in different ecosystems over Africa. *Remote Sensing of Environment, 114(2)*, 449-465. doi: 10.1016/j.rse.2009.10.002.

Wan, J. W., Yang, K., Zhang, W. J., & Zhang, J. L. (2009). A new method of determination of indoor temperature and relative humidity with consideration of human thermal comfort. *Building and Environment, 44(2),* 411-417. doi: 10.1016/j.buildenv.2008.04.001.

Wang, J., Yan, Z., Quan, X. W., & Feng, J. (2017). Urban warming in the 2013 summer heat wave in eastern China. *Climate Dynamics, 48(9)*, 3015-3033. doi: 10.1007/s00382-016-3248-7.

Weng, Q. (2009). Thermal infrared remote sensing for urban climate and environmental studies: Methods, applications, and trends. *ISPRS Journal of photogrammetry and remote sensing, 64(4)*, 335-344. doi: 10.1016/j.isprsjprs.2009.03.007.

WHO. (2020). Heatwaves. *World Health Organization*. doi: https://www.who.int/health-topics/heatwaves

Wiersema, D. J., Lundquist, K. A., & Chow, F. K. (2020). Mesoscale to microscale simulations over complex terrain with the immersed boundary method in the Weather Research and Forecasting Model. *Monthly Weather Review, 148(2)*, 577-595. doi: 10.1175/mwr-d-19-0071.1.

Wikipedia. Humidex. *In Wikipedia*: http://en.wikipedia.org/wiki/Humidex.

Wikipedia. Yangtze Delta. *In Wikipedia*. https://en.wikipedia.org/wiki/Yangtze_Delta

Wilson, O. (1967). Objective evaluation of wind chill index by records of frostbite in the Antarctica. *International journal of biometeorology, 11(1),* 29-32. doi :10.1007/bf01424272.

Rothfusz, L. P., & Headquarters, N. S. R. (1990). The heat index equation (or, more than you ever wanted to know about heat index). *Fort Worth, Texas: National Oceanic and Atmospheric Administration, National Weather Service, Office of Meteorology, 9023*.

Anderson, G. B., Bell, M. L., & Peng, R. D. (2013). Methods to calculate the heat index as an exposure metric in environmental health research. *Environmental health perspectives, 121(10)*, 1111-1119. doi: 10.1289/ehp.1206273.

Ravagnolo, O., Misztal, I., & Hoogenboom, G. (2000). Genetic component of heat stress in dairy cattle, development of heat index function. *Journal of dairy science, 83(9)*, 2120-2125. doi: 10.3168/jds.s0022-0302(00)75094-6

World Health Origanization (WHO). (2018). Heat and Health. *World Health Origanization.* https://www.who.int/news-room/fact-sheets/detail/climate-change-heat-and-health

Wyngaard, J. C. (1992). Atmospheric turbulence. *Annual Review of Fluid Mechanics, 24(1)*, 205-234. doi: 10.1146/annurev.fl.24.010192.001225.

Zakšek, K., & Schroedter-Homscheidt, M. (2009). Parameterization of air temperature in high temporal and spatial resolution from a combination of the SEVIRI and MODIS instruments. *ISPRS Journal of Photogrammetry and Remote Sensing, 64(4)*, 414-421. doi: 10.1016/j.isprsjprs.2009.02.006.

Zamanian, Z., Sedaghat, Z., Hemehrezaee, M., & Khajehnasiri, F. (2017). Evaluation of environmental heat stress on physiological parameters. *Journal of Environmental Health Science and Engineering, 15(1)*, 1-8. doi: 10.1186/s40201-017-0286-y.

Zhang, H., Zhang, F. A. N., Zhang, G., Ma, Y., Yang, K. U. N., & Ye, M. (2018). Daily air temperature estimation on glacier surfaces in the Tibetan Plateau using MODIS LST data. *Journal of Glaciology, 64(243)*, 132-147. doi: 10.1017/jog.2018.6.

Colombi, A., De Michele, C., Pepe, M., Rampini, A., & Michele, C. D. (2007). Estimation of daily mean air temperature from MODIS LST in Alpine areas. *EARSeL eProceedings, 6(1)*, 38-46.

Zhang, H., Zhang, F., Zhang, G., He, X., & Tian, L. (2016). Evaluation of cloud effects on air temperature estimation using MODIS LST based on ground measurements over the Tibetan Plateau. *Atmospheric Chemistry and Physics, 16(21)*, 13681-13696. doi: 10.5194/acp-16-13681-2016.

Zhu, X., Chen, J., Gao, F., Chen, X., & Masek, J. G. (2010). An enhanced spatial and temporal adaptive reflectance fusion model for complex heterogeneous regions. *Remote Sensing of Environment, 114(11)*, 2610-2623. doi: 10.1016/j.rse.2010.05.032.